Direct Observation of Broken Time-Reversal Symmetry on the Surface of a Magnetically Doped Topological Insulator

Yoshinori Okada,[1] Chetan Dhital,[1] Wenwen Zhou,[1] Erik D. Huemiller,[1] Hsin Lin,[2] S. Basak,[2] A. Bansil,[2] Y.-B. Huang,[3] H. Ding,[3] Z. Wang,[1] Stephen D. Wilson,[1] and V. Madhavan[1]

[1]*Department of Physics, Boston College, Chestnut Hill, Massachusetts 02467, USA*
[2]*Physics Department, Northeastern University, Boston, Massachusetts 02115, USA*
[3]*Beijing National Laboratory for Condensed Matter Physics, and Institute of Physics, Chinese Academy of Sciences, Beijing 100190, China*

(Received 20 January 2011; revised manuscript received 4 March 2011; published 17 May 2011)

We study interference patterns of a magnetically doped topological insulator $Bi_{2-x}Fe_xTe_{3+d}$ by using Fourier transform scanning tunneling spectroscopy and observe several new scattering channels. A comparison with angle-resolved photoemission spectroscopy allows us to unambiguously ascertain the momentum-space origin of distinct dispersing channels along high-symmetry directions and identify those originating from time-reversal symmetry breaking. Our analysis also reveals that the surface state survives far above the energy where angle-resolved photoemission spectroscopy finds the onset of continuum bulk bands.

DOI: 10.1103/PhysRevLett.106.206805 PACS numbers: 73.20.−r, 74.55.+v

When spin-orbit coupling is strong enough, a band-parity inversion can be generated around the direct conduction-valence band gap of an insulator. Such topological insulators (TIs) support gapless surface states that in the low-energy and long-wavelength limit have linear energy-momentum dispersions. The extraordinary properties of these Dirac surface states translate into a unique potential for new types of devices and for realizing novel physical phenomena [1–3]. Since massless Dirac fermions are helicity eigenstates, the states carry a helical spin texture; the electron's spin is normal to the direction of its lattice momentum. The constraints of time-reversal (TR) symmetry prohibit direct backscattering between the time-reversed pair of helicity eigenstates, which carry opposite momenta and spin and restore these channels when TR symmetry is violated. Direct experimental determination of scattering processes is important not only for establishing their predicted spin texture and its role within the protected surface phase but also for theoretical modeling of the physical properties of these materials. Intensive STM [4–7] and angle-resolved photoemission spectroscopy (ARPES) [8–10] studies have beautifully demonstrated many of the canonical properties including the absence of backscattering in TR invariant TIs. However, while the effects of magnetic impurities on bulk and surface band structures have been extensively studied [11–13], to date no direct observations of TR violating scattering vectors have been reported.

In this work, we probe the scattering processes in Fe-doped Bi_2Te_3 by the technique of using the Fourier transform of STM dI/dV maps (spectroscopic maps) to obtain q-space information (FT-STS) [14–16] to show the emergence of new scattering channels due to broken TR symmetry. Our Fourier transform STM data combine high momentum resolution [spatial maps with a minimum linear dimension of 1500 Å were used for the fast-Fourier transform (FFT)] with data over a large range of energy (up to 600 meV above the Dirac point). By comparing these high-resolution data to ARPES, we were able to distinguish the momentum-space (k-space) origins of the STM scattering vectors and show that the new channels arise from forbidden backscattering. With an unambiguous identification of the scattering channels, we find a surprising result: The dispersion at higher energies indicates the survival of the surface states well beyond the onset of the conduction band. This suggests that their topological nature may play an unexpected role in protection against the mixing with the bulk states beyond the insulating band gap.

We focus on Fe-doped Bi_2Te_3 single crystals with a nominal Fe doping of 0.25%, $(Bi_{1-x}Fe_x)_2Te_3$ ($x = 0.0025$). Sample preparation methods as well as ARPES and STM experimental details are described in Ref. [17]. Bi_2Te_3 belongs to a new generation of TR invariant 3D topological insulators of the type Bi_2X_3 ($X =$ Te, Se, etc.) whose discovery has been pivotal in this field [18–21]. Fe doping acts to locally break TR symmetry, which has many interesting consequences [22–26]. In Bi_2Te_3, warping of the surface state due to the threefold symmetric crystal potential and interaction with the bulk bands provides an enhancement of certain scattering channels over others, allowing them to be observed by STM. Bi_2Te_3 cleaves between the quintuple layers terminating in a Te surface [Fig. 1(a)]. For our studies, we have deliberately doped a dilute concentration of Fe atoms, which are expected to enter substitutionally in the Bi plane but may also appear as defects in the Te plane. FFT of the STM topography shows the hexagonal lattice associated with the Te atoms [Fig. 1(a), inset]. dI/dV spectra reveal a suppression of density of states near the Fermi energy (E_F) [Fig. 1(b)]. Although it is not straightforward to extract the

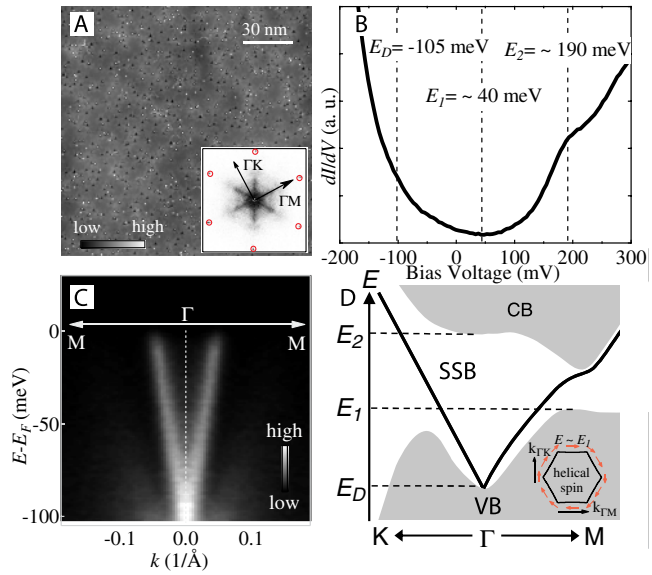

FIG. 1 (color online). (a) STM topography of $(Bi_{1-x}Fe_x)_2Te_3$ ($x = 0.0025$), linear dimension 1500 Å, showing the various triangle-shaped impurities and defects. Only atomic resolution tips were used for this study. The high-symmetry directions in k space are specified in the inset. All k-space figures are henceforth rotated such that ΓM is along the horizontal axis. (b) dI/dV spectrum showing the energies E_D, E_1, and E_2 schematically represented in 1D. E_D is from the STM data. The other two energies were extrapolated from prior ARPES [18]. (c) ARPES on samples from the same batch showing the Dirac point close to −100 meV. (d) Schematic of band structure and surface state showing: the Dirac point (E_D), the valance band top along ΓM (E_1), and the conduction band bottom (E_2) along ΓM. All data in this Letter are from maps on one sample. The other Fe-doped samples showed similar results. Energies are specified with reference to E_F ($E_F = 0$ meV).

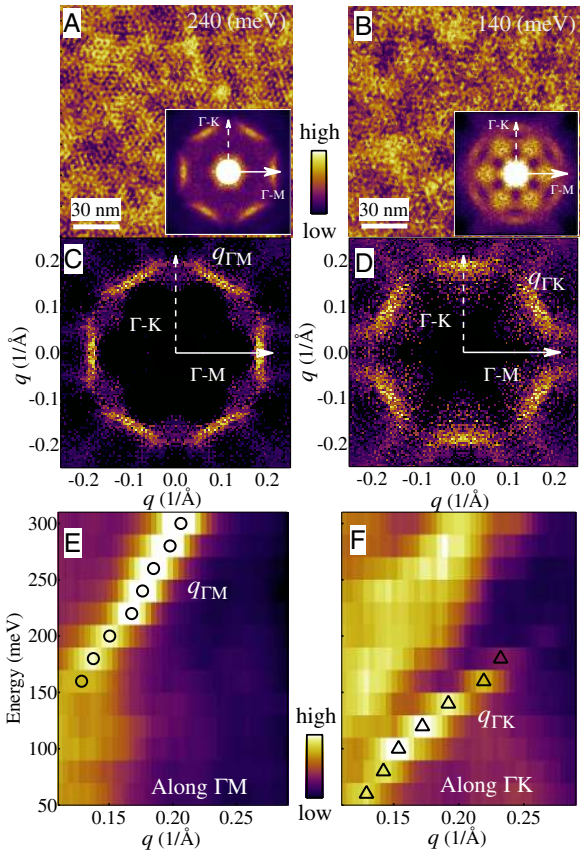

FIG. 2 (color online). (a),(b) dI/dV (r, E) maps showing the IPs with the inset showing the raw FFT. (c),(d) The same FFT as the insets but divided by FFT at +60 meV. FFT patterns are hexagonally symmetrized. (e),(f) Intensity profiles of the raw undivided FFTs (line cuts of FFTs along the specified direction, represented as a color intensity). These are plotted at various energies (vertical axis) along ΓM (e) and ΓK (f) and show the evolution of the q vectors, $q_{\Gamma M}$ (circle) and $q_{\Gamma K}$ (triangle) with energy. The additional broad feature at smaller q values in (f) is possibly due to a set of vectors close to q_4 (Fig. 3) and is not analyzed in any further detail.

position of the conduction or valance bands from the spectra, we will later show that the shape of the spectrum is consistent with the position of the bulk bands extrapolated from prior ARPES data.

To obtain the surface state dispersion, dI/dV (r, eV) maps were obtained at various energies. Similar to previous studies [5,6], interference patterns (IPs) emerge above a threshold energy in our samples [Figs. 2(a) and 2(b)]. At energies above +150 meV, we observe a sixfold symmetric pattern with intensity centered along the ΓM directions ($q_{\Gamma M}$) [Fig. 2(a), inset]. The ΓM scattering vector has been previously reported in STM studies of Bi_2Te_3 samples without TR symmetry breaking. There is as yet no consensus on its momentum-space origin, either theoretically [27–29] or experimentally [5,6]. Remarkably, at low energies starting around +60 meV, our data reveal a new set of scattering vectors (q vectors) centered along ΓK ($q_{\Gamma K}$) [Fig. 2(b), inset], not reported in prior STM studies [5,6]. Since the FFT shows nondispersive features at low energies, a division by the lowest-energy (+ 60 meV) FFT makes the patterns above this energy clearer [Fig. 2(d)] (see [17], Fig. S2, for evolution of raw FFT with energy).

Plotting the dispersion obtained from the raw undivided FFT along ΓM [Fig. 2(e)] and ΓK [Fig. 2(f)], we observe that their slopes are different. We now discuss the possible origin of these dispersive q vectors.

We first consider the q vectors along the primary directions ΓM and ΓK. While there are a multitude of scattering channels, a few of the special wave vectors, which connect stationary points in k space (labeled q_1–q_6), are shown in the inset in Fig. 3(a). q_3 and q_6 serve as upper bounds on the magnitude of q vectors in the ΓM direction and ΓK direction, respectively, while q_1 is a lower bound along ΓM. q_5 along ΓK and q_3 along ΓM are forbidden in the time-reversal invariant TI. In the presence of TR symmetry breaking Fe impurities, however, these vectors must be considered.

In order to identify the origin of $q_{\Gamma M}$ and $q_{\Gamma K}$, we compare STM dispersion to ARPES. Since the IPs occur above E_F in our samples, our ARPES data below E_F do not

capture this energy region. We therefore access the higher energy dispersion from previously published ARPES on Bi_2Te_3 [18]. We fit the ARPES dispersion along ΓM and ΓK (details in [17]) and use this to calculate q vectors as a function of energy. The resulting ARPES determined dispersions of the six q vectors (q_1–q_6) can now be rigidly shifted in energy to match STM data, as shown in Fig. 3(a).

Overlaying the ARPES q-vector dispersions on $q_{\Gamma M}$ and $q_{\Gamma K}$ [Fig. 3(a)], we find that the slope, direction, and magnitude of $q_{\Gamma M}$ and $q_{\Gamma K}$ strongly constrain the fit between ARPES and STM and determine the position of Dirac point as $E_D = -105 \pm 5$ meV, which is within the range of our independent ARPES data obtained on the same samples [Fig. 1(c)]. Extrapolating the relative energies of other band structure features from ARPES [Fig. 1(d)], we find that our spectral shape corresponds well with the band structure. We find a minimum in the density of states close to the valance band maximum and a van Hove feature associated with the conduction band minimum along ΓM. Interestingly, since a 3D band edge does not normally produce sharp features in the density of states, the van Hove feature associated with the bottom of the conduction band is due to the rather flat-band dispersion of the latter near the Γ point.

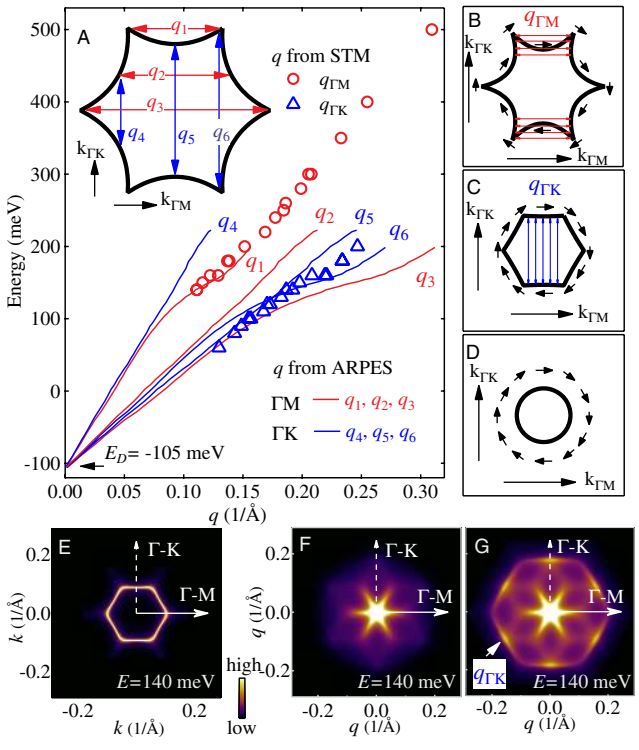

FIG. 3 (color online). (a) Dispersion of the six q vectors shown in the inset calculated from ARPES data [18] (solid lines) and shifted in energy to match the STM q vectors obtained from the FFT of the IPs (circles and triangles). The best match between STM and ARPES is obtained for a Dirac point of -105 meV. (b)–(d) Schematic of CECs and the nested regions of the CECs resulting in the primary q vectors observed in STM at low energies along ΓK and higher energies along ΓM. (e) Calculated CEC, (f) FFT including spin-texture-related matrix elements (TR invariant system), and (g) FFT with no spin-texture-related matrix elements (broken TR symmetry), at a representative energy of $+140$ meV.

From the dispersion in Fig. 3(a), $q_{\Gamma M}$ can be identified with scattering vectors close to q_1, a scattering channel not suppressed by the spin texture [Fig. 3(b)]. $q_{\Gamma K}$, on the other hand, originates from vectors close to q_5 and q_6, one of which (q_5) would be strictly forbidden in the time-reversal invariant TI. The appearance of these particular q vectors in STM can be understood by consulting the topology of the surface state band. From ARPES, the constant energy contours (CECs) of the surface state band change from an isotropic circular shape into a hexagon and then finally into the six-pointed shape of a snowflake [Figs. 3(b)–3(d)]. Assuming a rigid band shift of ARPES-determined energies, the transition from circular to hexagon-shaped CEC begins at approximately $+50$ meV, while the distorted snowflake shape appears near the bottom of the conduction band ($\sim +140$ meV). The first appearance of $q_{\Gamma K}$ ($\sim +60$ meV) therefore coincides with the transition from circular to hexagonlike CECs. In this regime, while q_5 and q_6 are only slightly different [Figs. 3(a) and 3(c)], $q_{\Gamma K}$ is a better match to q_5. An important point here is that these scattering vectors are enhanced at the stationary points of the distorted CECs [27] which provide nesting or near nesting conditions. The same is true for $q_{\Gamma M}$, which appears after the CEC distorts further from a hexagon into a snowflake ($> +140$ meV), where it arises from the most strongly nested regions [Fig. 3(b)].

To further clarify the k-space origin of the STM q vectors, we perform a model calculation of the expected FFT patterns both with and without spin-texture-related matrix elements (all possible scattering vectors allowed). We fit a $k \cdot p$ model [27] that captures the single Dirac-cone surface states centered at the Gamma point to ARPES data [18] (Fig. S3). This allows us to obtain numerical values for the parameters in the model (details in [17]). To calculate FFT patterns, we use the spin-dependent scattering probability:

$$\mathrm{SSP}(q) = \int_k A(k)T(q,k)A(k+q)dk,$$

where $A(k)$ is the spectral weight and $T(q, k)$ is a scattering matrix element.

We find systematic similarities between the STM and the calculated FFT patterns. The extended hexagon shape of the STM FFT patterns [Figs. 2(c), 2(d), and 4(a)] compare well with calculations [Figs. 3(g) and S4] and arise from small angle deviations from the primary scattering vectors which are still strongly nested. Importantly, we find that the STM data [Fig. 2(c)] are most consistent with the theoretical FFT with no spin-texture-related matrix elements [Fig. 3(g)]. In fact, spin-texture-related matrix element effects almost completely suppress $q_{\Gamma K}$ and the nearby vectors [Fig. 3(f)] observed in STM [Fig. 2(d)]. This provides strong support for the identification of the low-energy ΓK channel with broken TR symmetry scattering.

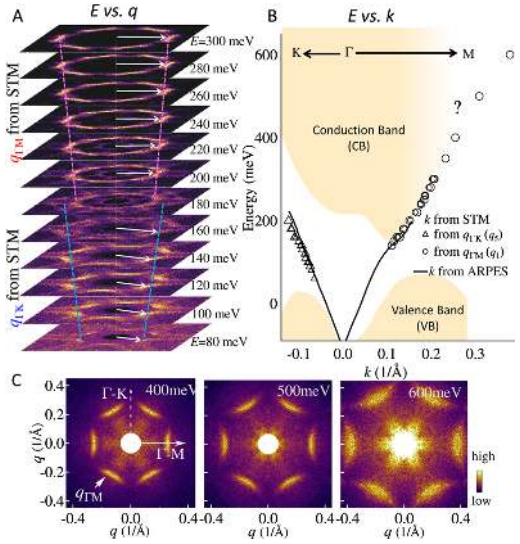

FIG. 4 (color online). (a) Energy evolution of STM q vectors. The FFTs are divided by the FFT at +60 meV. (b) Identifying the origin of the STM q vectors allows us to translate back into k space. The gray solid line is k-space dispersion extrapolated from ARPES data. Band structure is a schematic based on ARPES. From STM q vector $q_{\Gamma M}$ we obtain k along ΓM (black circles), which persists up to 600 meV above E_D, as also seen in (c). $q_{\Gamma K}$ may be associated with either q_5 or q_6 (Fig. 3), which have similar magnitudes when the CECs are almost circular. Associating $q_{\Gamma K}$ with q_5 we can calculate k along ΓK (black triangles). The correspondence with ARPES data indicates that the dominant channel at low energies is q_5. The deviation from linearity above ~160 meV energies indicates that we are beginning to see a mixture of q_5 and q_6.

With clear evidence of broken TR symmetry in our samples, we address the question of the origin of these processes. A single magnetic impurity mixes the TR paired states, thereby breaking TR symmetry locally. At the other extreme, long-range ferromagnetic order opens a gap at the Dirac point [11] and is expected to enhance forbidden scattering between time-reversed paired states, resulting in a stronger effect on the IPs compared to uncorrelated magnetic impurities. While our samples show no obvious bulk magnetization, local regions of ferromagnetically correlated domains or enhanced surface ferromagnetism mediated by the surface state electrons [11] may still exist.

Given the constraints on the surface state dispersion from ARPES and the exceedingly good agreement between STM and ARPES, the identification of $q_{\Gamma M}$ with the nested set of vectors q_1 is inescapable. This raises intriguing questions. As seen in ARPES, the tips of the snowflake become increasingly ill-defined at higher energies as the surface state enters the bulk band. Remarkably, we observe a linear dispersion for this set of vectors up to $\sim +600$ meV above the Dirac point well into the bulk conduction band [Figs. 4(b) and 4(c)]. This suggests that the surface states remain distinct (possibly as a resonance) over a surprisingly large energy range such that the bulk-surface mixing continues to be suppressed beyond the insulating gap. Another explanation for the survival of these states is that the higher-energy bulk bands deviate considerably from what we might expect based on ARPES data. The robustness of the surface state has important implications for its contribution to other properties of TIs as well as for applications. We expect that continued investigations via FT-STS within the higher-energy regime where the $q_{\Gamma M}$ dispersion deviates from linearity would provide important information on the high-energy electronic structure in topological insulators and serve as a vital complement to ARPES measurements currently precluded from probing this range.

This research was supported by U.S. NSF (CAREER-0645299 and 1056625), DOE (DE-SC0002554, AC03-76SF00098, and FG02-07ER46352), China 973 Program (2010CB923000), and Sino-Swiss Science and Technology Cooperation (SSSTC) and benefited from allocation of time at the NERSC and ASCC computation centers.

[1] X.-L. Qi, R. Li, J. Zang, and S.-C. Zhang, Science **323**, 1184 (2009).
[2] L. Fu and C. L. Kane, Phys. Rev. Lett. **100**, 096407 (2008).
[3] X.-L. Qi, T. L. Hughes, and S.-C. Zhang, Phys. Rev. B **78**, 195424 (2008).
[4] P. Roushan *et al.*, Nature (London) **460**, 1106 (2009).
[5] T. Zhang *et al.*, Phys. Rev. Lett. **103**, 266803 (2009).
[6] Z. Alpichshev *et al.*, Phys. Rev. Lett. **104**, 016401 (2010).
[7] J. Seo *et al.*, Nature (London) **466**, 343 (2010).
[8] D. Hsieh *et al.*, Nature (London) **460**, 1101 (2009).
[9] H. J. Zhang *et al.*, Nature Phys. **5**, 438 (2009).
[10] D. Hsieh *et al.*, Science **323**, 919 (2009).
[11] Y. L. Chen *et al.*, Science **329**, 659 (2010).
[12] L. A. Wray *et al.*, arXiv:1009.6216v1.
[13] Y. S. Hor *et al.*, Phys. Rev. B **81**, 195203 (2010).
[14] L. Petersen *et al.*, Phys. Rev. B **57**, R6858 (1998).
[15] M. F. Crommie, C. P. Lutz, and D. M. Eigler, Nature (London) **363**, 524 (1993).
[16] J. E. Hoffman *et al.*, Science **297**, 1148 (2002).
[17] See supplemental material at http://link.aps.org/supplemental/10.1103/PhysRevLett.106.206805 for details on crystal growth, data analysis and fitting parameters, and theoretical FFT calculations.
[18] Y. L. Chen *et al.*, Science **325**, 178 (2009).
[19] L. Fu, C. L. Kane, and E. J. Mele, Phys. Rev. Lett. **98**, 106803 (2007).
[20] J. E. Moore and L. Balents, Phys. Rev. B **75**, 121306(R) (2007).
[21] D. Hsieh *et al.*, Phys. Rev. Lett. **103**, 146401 (2009).
[22] M. T. Tran and K. S. Kim, Phys. Rev. B **82**, 155142 (2010).
[23] J. Chen *et al.*, Phys. Rev. Lett. **105**, 176602 (2010).
[24] H. T. He *et al.*, arXiv:1008.0141v1.
[25] X. L. Qi, T. Hughes, and S. C. Zhang, Phys. Rev. B **78**, 195424 (2008).
[26] K. Nomura and N. Nagaosa, Phys. Rev. B **82**, 161401 (2010).
[27] L. Fu, Phys. Rev. Lett. **103**, 266801 (2009).
[28] X. Zhou, C. Fang, W. Tsai, and J. Hu, Phys. Rev. B **80**, 245317 (2009).
[29] W. C. Lee, C. Wu, D. P. Arovas, and S. C. Zhang, Phys. Rev. B **80**, 245439 (2009).